Combined chemoresistive and *in situ* FTIR spectroscopy study of nanoporous NiO films for light-activated nitrogen dioxide and acetone gas sensing

Katarzyna Drozdowska [a,*], Tesfalem Welearegay [b], Lars Österlund [b], Janusz Smulko [a]

[a] *Department of Metrology and Optoelectronics, Faculty of Electronics, Telecommunications, and Informatics, Gdańsk University of Technology, G. Narutowicza 11/12, 80-233 Gdańsk, Poland*
[b] *Department of Materials Science and Engineering, The Ångström Laboratory, Uppsala University, P.O. Box 35, SE-75103 Uppsala, Sweden*

A B S T R A C T

The chemoresistive sensor response of nanoporous NiO films prepared by advanced gas deposition was investigated by combined resistivity and *in situ* FTIR spectroscopy, with and without simultaneous light illumination, to detect NO_2 and acetone gases. The sensitivity towards NO_2 increased dramatically under UV irradiation employing 275 nm light. Improved sensitivity was observed at an elevated temperature of 150 °C. *In situ* FTIR measurements were performed to record the transient gas adsorption/desorption processes. The sustained sensitivity and repeatability for NO_2 sensing could be attributed to reversible surface-nitro and nitrate species formation, which are stable on the surface at relative humidity up to 40%. In contrast, acetone sensing results in irreversible decomposition and accumulation of reaction products on the NiO sensor surface, covering the surface and limiting gas sensing. Implications of the study for improved and sustained NiO gas sensor properties in gas mixtures are discussed.

1. Introduction

Since the last decade, significant progress in gas sensing systems based on metal oxide semiconductors (MOS) has been made [1,2]. Primary attention was attracted to *n*-type semiconductors such as ZnO, SnO_2, WO_3, TiO_2, In_2O_3. Numerous studies focused on improving gas sensors based on *n*-type materials, including nanostructures fabrication, surface modifications, doping, or composites manufacturing [3–5]. In addition, their high sensitivity to various toxic gases and pollutants led to the production of commercially used devices for safety monitoring [6]. Simultaneously, *p*-type semiconducting metal oxides such as CuO, NiO, Cr_2O_3, Co_3O_4, or Mn_3O_4 have received much less attention, justified mainly by the lower gas sensitivity of these materials [7]. However, *p*-type semiconducting metal oxides offer several attractive properties for gas detection, such as lower working temperature and higher humidity tolerance compared to their *n*-type counterparts. In particular, a humidity-tolerant ultrathin NiO sensing layer for NO_2 detection was recently reported by Wilson et al. [8]. According to their results, NiO layers do not exhibit a significant change in their electrical properties up to 70% relative humidity (RH) at working temperatures between 50 and 200 °C.

High selectivity of *p*-type MOS sensors has been reported as well [9, 10]. The performance of the gas sensing layer is attributed not only to external parameters (operating temperature, humidity, electromagnetic radiation) but also to chemical composition, dopants, crystallinity, and morphology [11–13]. In the case of nanostructured NiO, selectivity towards NO_2, ethanol, and formaldehyde has been reported, showing that NiO-based devices may be efficient for detecting both oxidizing and reducing agents [8,14,15].

Several strategies have been reported for increasing the sensitivity of *p*-type MOS sensors, including tuning morphology, doping, loading with noble metals or metal oxides [10]. Apart from that, light-induced gas detection remains an attractive alternative to high-temperature sensing and can facilitate room-temperature operation [16–19]. The wide bandgap of NiO is reported to be about 3.6 eV [20], depending on the fabrication method and structural properties, thus restricts interband absorption to the wavelengths below 344 nm. However, specific synthesis routes and control of the morphology of NiO nanostructures may expand the light absorption range to the visible region. X. Geng et al. proposed precipitation and hydrothermal methods for obtaining black

NiO samples with high absorbance over the whole visible region [21]. Light-illuminated black NiO with a high concentration of Ni^{3+} ions, excess oxygen vacancies, and large specific surface area allowed ppb NO_2 detection level. This latter study shows that black NiO is a promising candidate for selective, sensitive, and low-cost gas sensing when the additional excitation source is used. Nevertheless, further investigations of their long-time repeatability in various conditions such as elevated temperatures, light illumination, and changing humidity require further elaboration.

Herein, we present and discuss the performance of nanoporous NiO resistive gas sensor prepared by advanced gas deposition methods. We investigate the sensor response at different operating temperatures, irradiation wavelengths, and RH for the detection of both the oxidizing molecule NO_2 and the nucleophilic acetone, extracting theoretical detection limits for NO_2. Results of electrical measurements are complemented by *in situ* Fourier-transform infrared spectroscopy (FTIR) measurements, unraveling the surface reactions and dominant surface species responsible for the changed electrical properties of the NiO layers upon gas exposure.

2. Materials and methods

2.1. NiO films fabrication – AGD deposition

Nanoporous polycrystalline NiO films were deposited on silicon (Si) substrates by means of an advanced gas deposition (AGD) method [22], employing an Ultra-fine Particle system (ULVAC Ltd., Japan). The gas deposition technique is based on the evaporation of a pure metallic Ni pellet (purity, 99.9%) which is inductively heated inside a vacuum chamber held at pressure, P_1 (162 mbar), to produce a vapor pressure above the metal melt [22,23]. Introducing a mixture of cooled laminar flow of He (20 L/min) and O_2 (0.1 L/min) gases causes the vaporized metal atoms to condense and form nanoparticles with a well-defined log-normal size distribution. The nanoparticles are then transported into an upper vacuum chamber held at a lower pressure, P_2 (3.51 mbar), *via* a 3 mm diameter transfer pipe, as a result of pressure differences between the evaporation and the deposition chambers ($P_1 > P_2$). Thus, a stream of nanoparticles impinges on the Si substrate mounted on an XYZ stage motor positioned in the deposition chamber. During the fabrication and deposition of porous NiO films, the induction power of the coil was 3.4 kW (controlling the metal vapor pressure), the XYZ stage speed was set to 1.25 mm/s in each cycle, and three deposition cycles were employed to achieve the desired film properties (thickness, particle size). The laminar flows of the gases He and O_2 in the deposition chamber were kept constant at 20 L/min and 100 mL/min, respectively. The as-deposited sensor films were subsequently annealed at 400 °C for 12 h under synthetic air (S.A.) flow to consolidate the particle morphology and structure without allowing particle growth and significant loss of porosity [24]. The films thus obtained show *p*-type conductivity and the carrier density measured by van der Pauw method was determined to be 1.4×10^{16} cm^{-3} at 390 K (relevant for the temperatures employed in the gas sensor measurements). The measured carrier density is in the lower range reported for NiO films prepared by pulsed vapor deposition [25], which is expected due to extreme nanoporosity of the AGD prepared NiO films employed here.

2.2. Structural and chemical characterization

The structure and surface morphology of the NiO films was characterized by scanning electron microscopy (SEM; Zeiss LEO 1550) and by X-ray diffraction (XRD) by a Siemens D5000 diffractometer employing a CuK$_\alpha$ source ($\lambda = 1.5418$ Å) and diffraction angle of 2θ in the range 20–80°. Surface topography and film thickness were measured by surface profilometry (Bruker Dektak XT).

The surface oxidation state of the nanoporous NiO films was investigated by X-ray photoelectron spectroscopy (XPS) using an Ulvac PHI

Quantera II instrument. The binding energy was calibrated from the C—C contribution due to the C1s adventitious carbon signal at 284.8 eV. The pass energy was set to 224 eV and energy resolution of 0.8 eV for the survey scans, and pass energy of 55 eV at 0.2 eV energy resolution for the high-resolution elemental scans. The atomic O/Ni and C/Ni concentration ratios were determined to be 1.57 and 0.13, respectively.

2.3. In situ FTIR measurements

Fourier-transform infrared (FTIR) transmission measurements were performed on a vacuum pumped spectrometer (Bruker IFS 66v/S) equipped with a transmission reaction cell. *In situ* gas exposure, FTIR measurements were performed on NiO films coated on CaF$_2$ from the same batches as those prepared on Si substrates. In the FTIR measurements, the same exposure conditions were used as in the sensing measurements allowing analysis of the surface species being formed in the course of each gas exposure. The IR light was collected with a liquid nitrogen MCT detector. Repeated FTIR spectra were recorded with 4 cm^{-1} resolution. Each spectrum was averaged over 120 scans, yielding time series of spectra separated by about 30 s. The sample was first annealed at 400 °C under 50 mL/min S.A. flow for 1 h. Subsequently, the sample was cooled to 150 °C for FTIR measurement (operating temperature in the sensor measurements). In the *in situ* FTIR experiments, the NiO film first was exposed to S.A. for 1 h to allow the system to equilibrate, then 20 ppm of NO_2 was admitted for 10 min, followed by purging in S.A. For acetone measurement, S.A. was passed through a custom-made gas generator consisting of a capillary tube filled with pure liquid acetone (analytical grade, VWR Chemicals) kept in an insulated temperature-controlled box held constant temperature of 30 ± 0.2 °C, yielding about 1200 ± 100 ppm acetone in the feed gas [26]. Again, the NiO sample was kept in a flow of S.A. for 1 h at 150 °C followed by acetone dosing for 10 min while recording FTIR spectra.

2.4. Electrical measurements

The NiO sensor was placed onto a heater and attached as a component with variable resistance to the electrical circuit. Operating temperatures of 100 and 150 °C for gas sensing experiments were regulated by applying voltage to the heater. The sensor was driven by a voltage source with voltage U_0 in series with a driving resistance R_L in the applied circuit. During all measurements, the sensor was kept in a glass gas chamber. The electronic circuit was placed inside a metal box for shielding against external electromagnetic radiation. LEDs of different wavelengths within UV and visible range (275, 370, 470, and 660 nm) were positioned approximately 0.5 cm from the sensor surface. The optical power density was calculated as (0.13–0.19) mW/cm^2, (0.07–0.15) mW/cm^2, (1.70–2.50) mW/cm^2, and (0.97–2.60) mW/cm^2 for red, blue, UV 370 nm, and UV 275 nm, respectively. The values were evaluated based on the nominal optical parameters of the LEDs. For more details, Table S1 presents optical parameters and types of the LEDs used during gas sensing experiments.

A digital multimeter (Keithley 2002) was used for DC voltage measurements. The applied DC voltage U_0 and the measured sensor voltage U_S were collected and used for the calculation of the sensor resistance R_S according to the formula:

$$R_S = R_L \frac{U_S}{U_0 - U_S}. \tag{1}$$

2.5. Gas sensing experiments

Changes of the sensor DC resistance R_S were monitored for selected concentrations of NO_2 and acetone gas. In this work, the sensor response is presented as the following ratio:

$$\frac{R_S - R_0}{R_S}, \tag{2}$$

where R_0 denotes sensor baseline resistance in synthetic air (S.A.) or nitrogen (N_2) carrier feed gas. The analytic gas (NO_2 or acetone) was introduced into a gas chamber after diluting in the carrier gas. Humidity was added into the chamber by flowing the dry S.A. through a container filled with deionized water. The relative humidity (RH) was estimated using a commercial humidity sensor located in the gas chamber. RH value was established at room temperature (RT ≈ 23 °C) prior to the measurement (before heating or illumination), after introducing humid S.A. into the gas chamber for about 40 min. Mass flow controllers (Analyt-MTC, model GFC17) were used to set target gas concentrations. The gas mixture flow rate was kept between 100 and 150 mL/min to limit turbulent flow, and consequently, an additional source of fluctuations.

2.6. Detection limit estimation

The theoretical limit of detection (DL) was calculated based on relative sensor resistance changes at different concentrations of NO_2 under selected lighting conditions. A third-order polynomial function was fitted to the experimental data points. The deviation between experimental and theoretical values of the sensor response was used to estimate root mean square (RMS) value. Additionally, a linear fit was performed for the quasi-linear region of the sensor responses observed at low concentrations of NO_2 (2–8 ppm). Based on the calculated RMS and slope (from the linear fitted function), DL was determined according to the formula:

$$DL = \frac{(S/N) \cdot RMS}{slope}, \tag{3}$$

where S/N refers to the signal-to-noise ratio and is set to $S/N = 3$. As a signal, we refer to the relative changes of the sensor resistance according to (2).

3. Results and discussion

3.1. Structural and chemical characterization of NiO films

Fig. 1a shows X-ray diffractogram of NiO film annealed at 400 °C for over-night with a film thickness of 800 nm. As inferred from the diffractogram, pronounced peaks indicated at $2\theta = 37.4°$, $43.3°$, $62.9°$, and $75.6°$ confirmed the deposition of a well-developed polycrystalline NiO film in its cubic fcc structure (ICDD: 00-047-1049) with a corresponding preferred orientation of reflection planes assigned to (111), (200), (220),

and (311), respectively. A Scherrer analysis of (200) reflection yields a grain size of 6.4 nm. The XRD results presented here are consistent with our previously reported NiO films fabricated employing AGD [24].

Fig. 1b shows a typical SEM image of a NiO film exhibiting highly porous surface morphology consisting of sparsely packed sub-10 nm features (on the average 8 nm by analyzing several SEM images), which are of the same order as the grain size obtained from XRD (6.4 nm). Considering that the AGD technique yields isolated nanoparticles formed in the source chambers that are carried in a gas stream to hit the substrate in the deposition chamber, these results strongly suggest that the observed features in SEM represent crystalline NiO nanoparticles.

Fig. 2 shows XPS spectra of NiO films. The characteristic Ni2p doublet binding energies for NiO due to the complex intra-atomic multiple contributions of Ni^{2+} and Ni^{3+} ions appear at 854.06 eV and 856.06 eV, respectively, in good agreement with previous studies [24, 27]. Similarly, the O1s binding energy region exhibits the typical peaks due to O associated with NiO and Ni^{3+} or defects, respectively, with a relative larger intensity ratio for O in the NiO structure in good agreement with our previous results for post-annealed NiO films prepared by AGD [24].

3.2. Chemoresistive sensor measurements

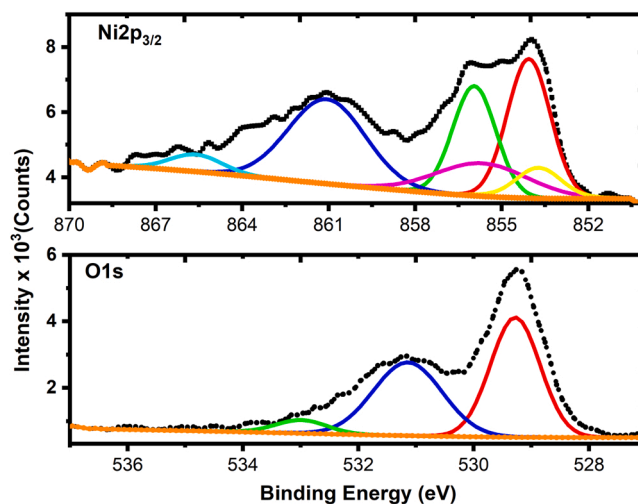The NiO gas sensor response was measured and compared under

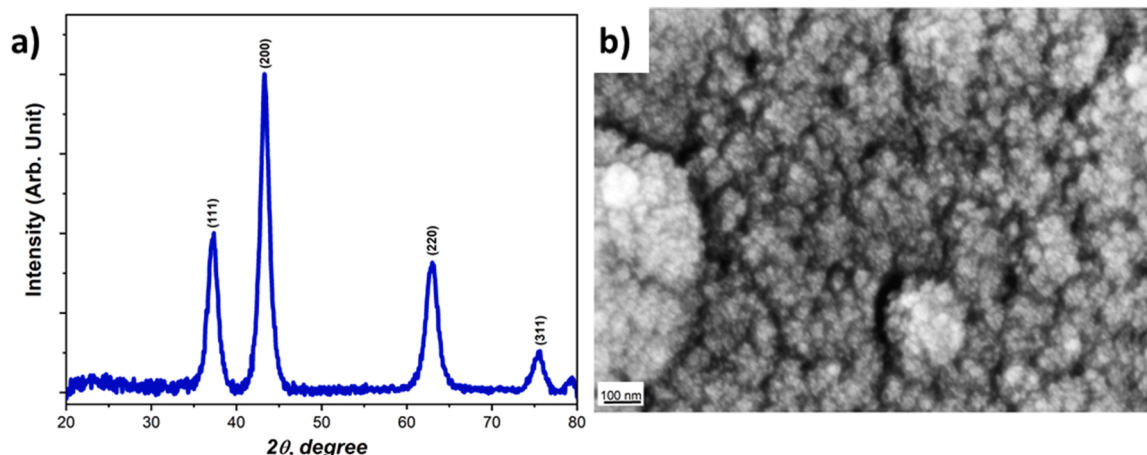**Fig. 2.** High-resolution Ni2p$_{3/2}$ and O1s XPS spectra of NiO films prepared by AGD.

Fig. 1. (a) X-ray diffractogram for 0.8 μm thick porous NiO film annealed at 400 °C, and (b) SEM surface analysis of NiO film.

selected operating conditions. The operating temperature is one of the parameters that strongly affect MOS sensors performance by significantly accelerating surface reactions [13]. Moreover, additional light illumination can enhance the gas detection process as well. Therefore, these two parameters and their impact on the NiO sensor performance were initially investigated. Initial measurements at room temperature (RT) in dark and with additional light irradiation did not give any sensor response in the dry or humid carrier gas. Hence, elevated working temperatures were used in the further investigation of the sensing properties of the device. Fig. 3a depicts the sensor resistance at selected concentrations of NO_2 and the operating temperature of 100 °C. Each cycle of introducing analytic gas (at concentrations 2–16 ppm) and returning to S.A. lasted approximately 15 min. These short-time gas pulses show the concentration-dependent dynamic response of the NiO sensor to NO_2. Each type of irradiation measurement yields different baseline sensor resistance, and this effect is the most visible for UV 275 nm LED. The drop of layer resistance in the presence of NO_2 confirms the *p*-type behavior of NiO, considering NO_2 is an oxidizing agent (electron acceptor). Light illumination affects the sensor behavior, reflecting higher responses for irradiated NiO sensors. See Fig. S1a, which shows the relative changes of sensor resistance at 100 °C, in the presence of NO_2 and under selected lighting conditions. The most significant changes can be observed for the UV LED of the shorter wavelength (275 nm), which hints that bandgap illumination is responsible for the signal since the bandgap of NiO is about 3.6 eV (344 nm) [20] and thus only accessible with the 275 nm LED. The red, blue, and UV 370 nm LED effect remains very similar at selected concentrations of NO_2. Simultaneously, the specified time required for the full recovery of the sensor is insufficient regardless of LED used; hence a short-time drift can be seen in Fig. 3.

Since the UV 275 nm LED is observed to enhance the sensing process, it was chosen for further measurements. Fig. 3b illustrates that the increase of the sensor operating temperature to 150 °C led to a significant enhancement of the relative resistance change. See also Fig. S1b for comparison of relative changes of sensor resistance at 100 and 150 °C. Compared with 100 °C, the NiO layer is characterized by more than eight times higher response at 150 °C even without additional illumination. At the same time, for the UV-assisted measurements (using 275 nm LED), the response raised approximately five times at 150 °C compared with 100 °C. This suggests that the NiO temperature and bandgap illumination have similar effects on the sensor signal, but that the signal shows a stronger temperature dependence, making it dominant at 150 °C. Fig. 4 summarizes the results obtained for short-time dynamic measurements, and is also the basis for the theoretical
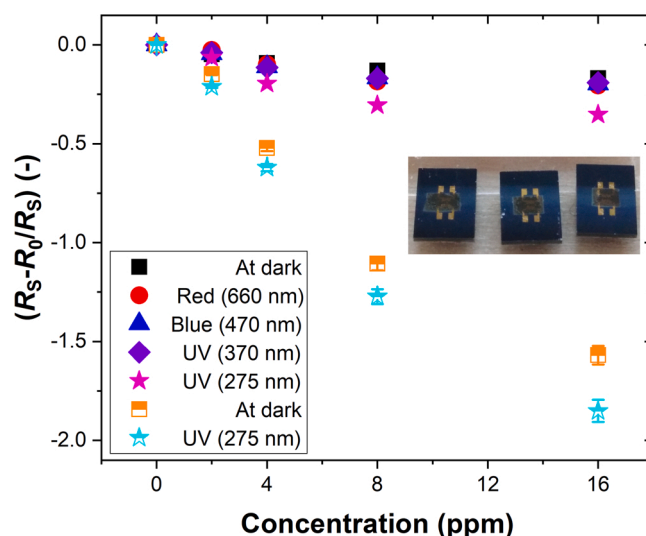

Fig. 4. Summary of relative changes in sensor resistance as a function of NO_2 concentration under different lighting conditions. Filled symbols refer to 100 °C working temperature, and half-filled symbols depict 150 °C conditions. The changes in non-irradiated and UV-irradiated sensor response exceed the recorded low variance in response ($\sim 3\%$) when the experiment was repeated several times for the same NO_2 concentration at 150 °C (indicated by error bars). The photograph in the inset shows fabricated NiO sensors.

detection limit (DL) estimation following the description provided in Section 2. Fig. S2 shows the sensor responses to different concentrations of NO_2 and fitting curves used to estimate DL. The operating temperature of 150 °C resulted in a lower DL: DL = 664 ppb in dark and DL = 525 ppb with additional UV illumination (UV 275 nm). For comparison, at 100 °C, DL was estimated to be 3.3 ppm for non-illuminated and 1.2 ppm for the UV-assisted sensor. The illumination with UV 370 nm, blue, and red LED provided similar DL values, DL ≈ 1 ppm. Overall, the higher temperature and UV 275 nm-assistance led to over 6-times lower DL.

See Table S2, which summarizes the DL values at all conditions examined during the short gas pulse measurements. We stress that the DL values reported here should be regarded as higher limits since measurements at NO_2 concentrations below 1 ppm were not possible with the current gas-flow distribution setup, and non-linear response for NiO gas sensors previously has been reported [28].

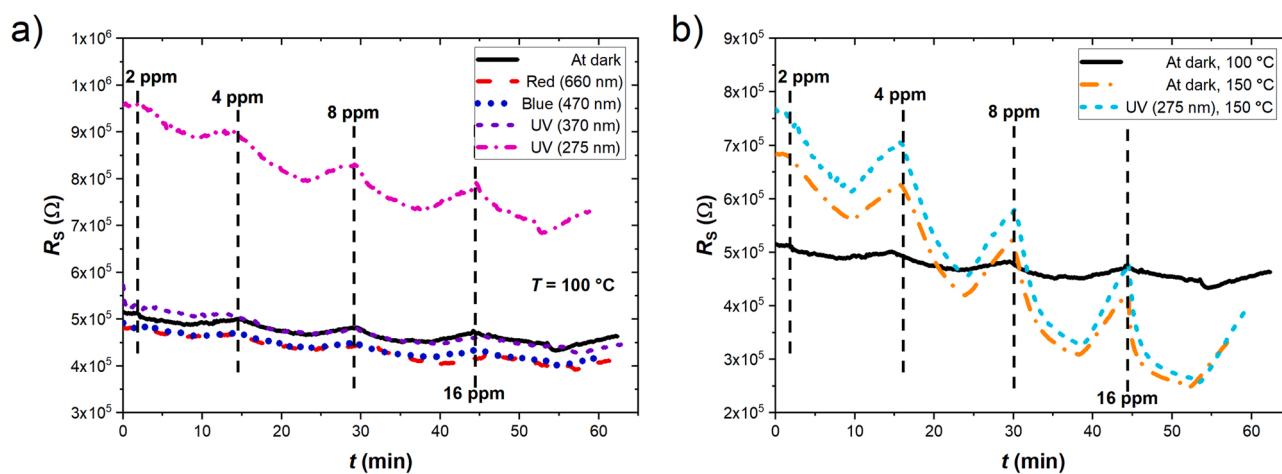The long-time dynamic responses of the sensor to NO_2 and acetone

Fig. 3. NiO sensor resistance in the presence of NO_2: (a) at the temperature of 100 °C in the dark and under illumination with red (660 nm), blue (470 nm), and UV (370 nm and 275 nm) LEDs, and (b) the comparison with device response at 150 °C both without UV and with additional UV (275 nm) LED irradiation. Vertical black dashed lines denote the time of introducing selected concentrations of a target gas.

were also investigated. The extended measurement time allowed a more precise evaluation of the gas sensing mechanism of the NiO layer. The studies were conducted at 150 °C. Fig. 5a presents the sensor resistance R_S in the presence of 30 ppm acetone and 4 ppm NO_2, respectively, at various conditions (carrier gas, relative humidity, UV irradiation).

In acetone gas, R_S exhibits a slow drift upwards, whereas the response to NO_2 results in a faster and pronounced decrease of R_S. We want to highlight that in the case of acetone, no visible sensor response was observed either at RT or 100 °C in the concentration range of 2–30 ppm. See Fig. S3, which confirms weak sensor performance towards selected concentrations of acetone at 100 °C, as an example. For 150 °C, we observed only a slow drift upwards for 30 ppm (as depicted in Fig. 5a). Lower concentrations of acetone did not produce visible sensor responses at such temperature. Since we observed that heating, irradiation, or humidity only change the baseline resistance of a sensor but not the response to acetone, we provide only one result concerning long-time drift of sensor resistance in 30 ppm of acetone. Elevated temperatures or irradiation with different LEDs only altered the sensor baseline resistance but did not improve acetone detection. In the case of NO_2, replacing S.A. with N_2 carrier gas results in a slower decrease of R_S. Stabilization of the resistance takes more than 100 min when NO_2 is diluted in N_2. Humidity (40% relative humidity, RH) has a similar but much less pronounced delaying effect, which can be seen in a close-up in Fig. 5b. The effect of UV illumination is not significant after about 10 min and indicates that irradiation promotes the surface reaction but does not alter the long-time product distribution. After approximately 50 min, the R_S reaches the saturation level in 4 ppm of NO_2 diluted in S. A. Estimated sensor response time values (considered as the time after which the sensor reaches 90% of R_S value at saturation) are summarized in Table S3. Noticeably, the sensor response time was shorter for the 4 ppm NO_2 gas under UV (275 nm) irradiation.

Fig. 6 presents the reproducibility of the NiO sensor response to 4 ppm of NO_2 following three cycles of NO_2 exposure (red solid curve) and three cycles of UV 275 nm light illumination (cyan dashed curve). In the latter case, the sensor resistance was first stabilized for 75 min in 4 ppm of NO_2 diluted in S.A. before the first cycle of irradiation. Clearly, the sensor response to 4 ppm of NO_2 is reproducible in each cycle. A similar R_S of approximately 3.5×10^5 Ω is reached in each cycle of introducing NO_2. However, 60 min is not sufficient for the full recovery of the sensor in both cases considered here, resulting in a long-term drift of the resistance between the consecutive cycles (about 20%). Moreover, additional UV light illumination, introduced after the sensor is stabilized in NO_2, does not have any noticeable effect, which is expected from the results presented in Fig. 5, showing the negligible influence of UV light after 10 min NO_2 exposure.
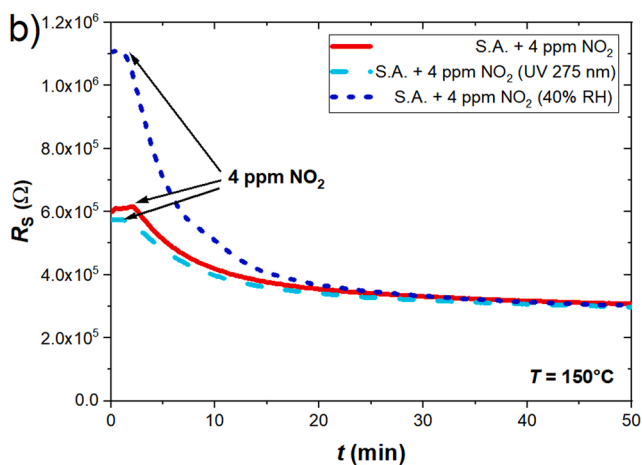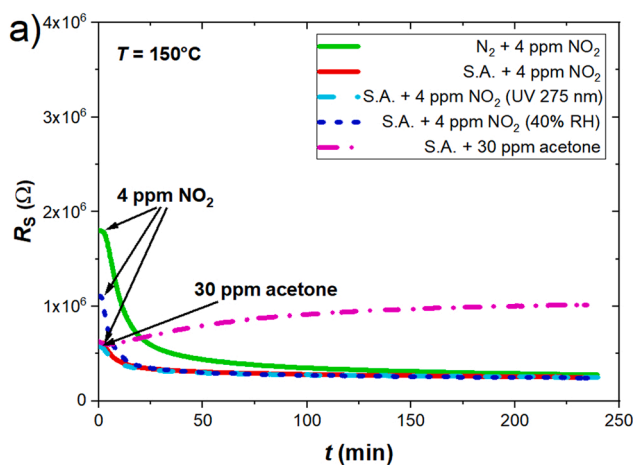

Fig. 6. The reproducibility of NiO sensor for three cycles of 4 ppm of NO_2 exposure in S.A.: (red solid curve) and UV 275 nm illumination (cyan dashed curve). The measurements were conducted at 150 °C in dry S.A.

Nanoporous NiO sensors prepared by AGD show a significant response towards NO_2. The operating temperature and different light illumination conditions significantly affect the electrical response of the sensor. At a sensor temperature of 150 °C, the sensor response is significantly enhanced compared to lower operating temperatures and allows for reproducible high-ppb NO_2 gas detection. Most metal oxide semiconductor (MOS) gas sensors require high operating temperature, usually in the range of 200–500 °C [3,29], although results of room temperature sensing using nanostructured NiO recently have been reported [28]. In general, the sensor response is accelerated at high operating temperature, but it comes at the cost of energy consumption and thermal management of the sensor device. Fig. 3, along with DL estimations, proves that heating up to 150 °C leads to stabilized and faster response and recovery on nanoporous NiO. At the same time, the NiO sensors were stable in relative humidity up to 40%, which suggests the less humidity-dependent properties of *p*-type MOS. Additionally, we highlight that experiments at various RH would further confirm a much less sensitivity towards water of *p*-type MOS sensors.

3.3. In situ FTIR measurements

FTIR measurements were used to characterize surface adsorption and reactions of NO_2 and acetone on the NiO film under similar conditions as those performed in the chemoresistive sensor measurements.

Fig. 5. (a) The change of the sensor resistance R_S in the presence of acetone or NO_2 gas in different reaction environments: carrier gas (S.A., or N_2), relative humidity (40% RH in S.A.), and UV irradiation (275 nm LED). (b) Close-up of selected data presented in (a). All measurements were conducted at 150 °C.
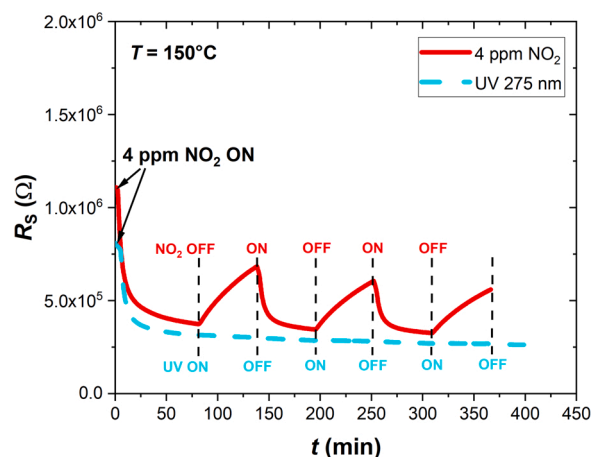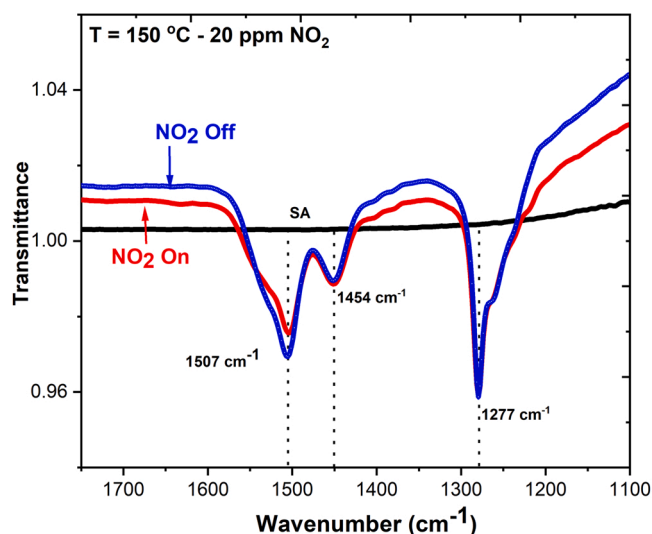
Fig. 7. *In situ* transmission FTIR spectra recorded during and after 20 ppm of NO$_2$ dosing in S.A. on nanoporous NiO film at 150 °C.

Fig. 7 shows FTIR spectra recorded after 1 h of flow in 100 mL/min dry S.A., followed by 10 min of 20 ppm NO$_2$ dosing in S.A. while keeping the sensor at a constant temperature of 150 °C. Major absorption bands occurring at 1507 cm^{-1}, 1454 cm^{-1}, and 1277 cm^{-1} were observed during NO$_2$ dosing. The two strong bands that appeared at 1507 cm^{-1} and 1277 cm^{-1}, which follow synchronous kinetics, can be associated with the asymmetric and symmetric N-O stretching modes in nitro species adsorbed on the NiO surface. The observed frequencies are shifted compared with its gas-phase value (ν_a(N-O) at 1610 cm^{-1} and ν_s(N-O) at 1325 cm^{-1}) [30], indicating appreciable interaction with NiO, possibly suggesting a bidentate NO$_2$ binding configuration. The band at 1454 cm^{-1}, which exhibits different temporal formation characteristics seen in Fig. 7, can be assigned to the ν_2(a$_1$) mode in a C_{2v} nitrate ion species, which either is monodentate or bidentate nitrate species bonded to surface Ni cations through the O atoms [31]. The spectral bands due to the surface-nitro species continue to increase a short time after closing the NO$_2$ gas supply, indicating diffusion and further rearrangement of NO$_2$ in the nanoporous NiO film into thermodynamically favorable sites. Previous theoretical studies have shown that the interaction of NO$_2$ with the NiO surface becomes stronger as the coverage increases [32], which would suggest chemical shifts of the stretching frequencies. The results presented in Fig. 7 give, however, no clear support for this prediction. Instead, high and low-frequency shoulders of the 1507 cm^{-1} and 1277 cm^{-1} bands, respectively, become more pronounced and could suggest a redistribution of bidentate to monodentate species according to Deacon's rule [33].

It has been suggested that NO$_3^-$ and NO$^+$ are formed on transition metal oxide surfaces through a disproportionation reaction (reaction (4)), *viz.* [31,34–36]:

$$3NO_{2,ads} + O_{surf}^{2-} \rightarrow NO_{3,ads}^- + s\text{-}NO_3^- + NO_{gas}, \tag{4}$$
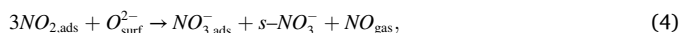
where s-NO$_3^-$ denotes a surface coordinated NO$_2$ species, where a lattice O surface atom is bonded to the N atom in NO$_2$, *i.e.*

$$NO_2^- + O_{lattice} \rightarrow s - NO_3^-, \tag{5}$$

leading to a formal nitro species. Although different reaction pathways leading to the surface nitrate and NO formation have been suggested [34–36], it is generally agreed that both surface nitro species and nitrate ions (NO$_3^-$) are present on the surface, both of which are detected in the present work (Fig. 7). The combined electrical and *in situ* FTIR measurements clearly show that NO must desorb from the surface in an NO$_2$ containing atmosphere to reach the steady-state situation shown in

Fig. 5 with a quasi-constant concentration of nitro and nitrate surface species (Fig. 7), consistent with reaction (4).

Considering that NO$_2$ is a strongly oxidizing species, with electron affinity significantly higher (2.27 eV) than O$_2$ (0.45 eV), displacement of some of the chemisorbed oxygen species from the surface is possible. This reaction is promoted by bandgap illumination, where reduction of Ni cation and surface nitro formation and proceeds *via* reaction (5) by oxidation of reduced oxygen and concomitant reduction of NO$_2$, *viz.*:

$$NO_{2,gas} + O_{lattice} + O_{2,ads}^- \rightarrow s - NO_{3,ads}^- + O_{2,gas}, \tag{6}$$
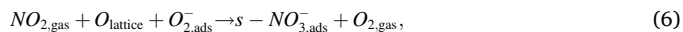
Also, the formation of nitrate is facilitated by bandgap illumination, *viz.*:

$$2NO_{2,gas} + 2O_{2,ads}^- \rightarrow 2NO_{3,ads}^- + O_{2,gas}, \tag{7}$$
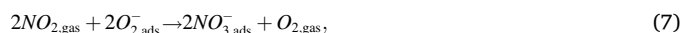
Therefore, reactions (6) and (7) can be responsible for the faster decrease of the resistance upon UV 275 nm illumination compared with the thermal oxidation reaction seen in Figs. 3 and 5. Reactions with adsorbed water would compete with reactions (5) and (6) and thus retard the nitro and nitrate formation. Hence, the resistance drop upon NO$_2$ exposure would be slower in a humid atmosphere, which is also observed in Fig. 5.

When the NiO layer is exposed to air, O$_2$ readily adsorb on the NiO surface. Depending on the operating temperature, dominant ions are reported to be O$_2^-$ up to 100 °C, O$^-$ in the temperature range 100–300 °C, and O^{2-} above 300 °C [37]. Regardless, oxygen adsorption leads to extraction of electrons from the material resulting in hole accumulation layer (HAL) formation and resistance decrease. In the presence of NO$_2$, a strong oxidizing agent, nitro and nitrate species are chemisorbed on the surface and displace O$_2$ (reactions (6) and (7)), leading to increased electron extraction and a further drop of the sensor resistance. The proposed mechanism is further supported by the results obtained when replacing synthetic air with N$_2$ carrier gas. Fig. 5a clearly shows that the sensor resistance decreases significantly slower in the presence of inert gas, supporting the interpretation above that interaction between NO$_2$ and adsorbed oxygen, yielding nitro and nitrate formation on the NiO surface, leads to the enhanced resistance decrease. Adsorbed water impedes the nitro and nitrate formation and retards the resistance drop but otherwise does not change the overall surface reactions due to the high electronegativity of NO$_2$ that thermodynamically favors nitro and nitrate formation.

Furthermore, light illumination promotes the surface nitro and nitrate formation on NiO. Black NiO (reduced NiO) absorbs light from UV to visible range efficiently. Similarly, our results show that any LED light from UV to red improved the response to NO$_2$ compared to dark conditions at 100 °C (Fig. 3a). The most significant change was observed for UV 275 nm with the shortest LED wavelength and the highest optical power density. Considering the bandgap of NiO, this was also the only LED with energy larger than the bandgap energy for stoichiometric NiO. This suggests that interband transitions in the NiO nanocrystals play a vital role in accelerating surface reactions. In the case of NO$_2$ adsorption, *in situ* FTIR shows that nitro and nitrate surface species are formed. It is known that surface nitrate formation is limited by charge transfer reactions from the metal cation. Here, bandgap absorption can promote this process by reducing Ni surface atoms to form surface nitro species, as indicated in Fig. 3a. A qualitatively similar explanation was proposed for NO$_2$ sensing using SnO$_2$ nanowires by Hung et al. [38]. In contrast, further adsorption and desorption of oxygen and its reaction with nitrate species do not affect the long-time sensor response when a saturated nitro and nitrate surface is formed, as shown in Fig. 5.

In situ transmission FTIR measurements were also performed with acetone gas in synthetic air exposures. Fig. 8 shows FTIR spectra obtained on porous NiO films during S.A., acetone dosing, and cleaning surface processes. The characteristic acetone vapor spectral bands at 1740 cm^{-1} (ν(C=O)) and 1226 cm^{-1} (ν(C-C)) are clearly seen during dosing as follows. These bands disappear when acetone is removed from
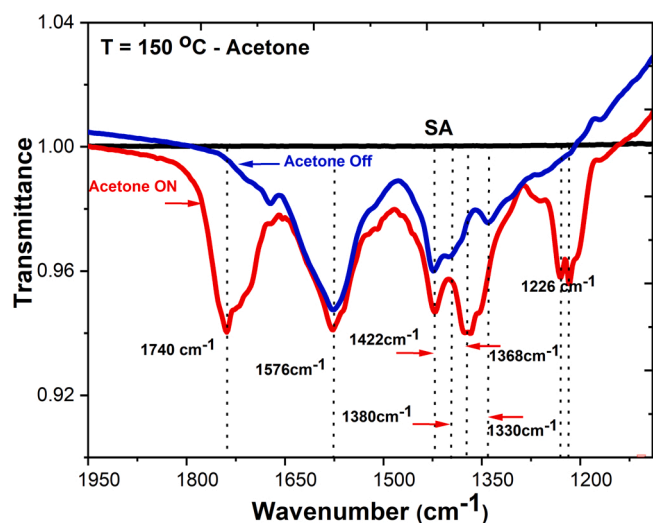
Fig. 8. *In situ* transmission FTIR spectra recorded during and after acetone dosing on nanoporous NiO film at 150 °C.

the feed gas, and only major bands at 1576 cm^{-1}, 1422 cm^{-1}, and 1380 cm^{-1} remain. These latter bands are due to formate (asymmetric and symmetric ν(CO) modes at 1576 cm^{-1} and 1330 cm^{-1}, respectively) and methoxy species (δ(CH) and ρ(CH) modes at 1380 cm^{-1} and 1422 cm^{-1}, respectively) that form upon acetone dissociation [31,39]. Thus, in contrast to NO$_2$, acetone adsorption leads to irreversible acetone decomposition and formate- and methoxy-covered surface formation. A gradual increase of the resistivity seen in Fig. 5a can thus be assigned to the gradual depletion of hole carriers in NiO due to nucleophilic bonding of formate and methoxy species on the NiO surface. Acetone dissociates on NiO and form strongly bonded surface species that reacts with NiO and depletes the hole carrier concentration, eventually deactivating the surface for further gas adsorption. It is therefore conjectured that for NiO to efficiently work as a gas sensor with sustained responsivity in realistic gas mixtures, our work suggests that efficient oxidation co-catalysts (*e.g.,* Pd or Pt) should be added to NiO to maintain its promising NO$_2$ sensing properties, exhibiting sub-ppm DL, humidity tolerance, as well as UV signal and time responsivity enhancement.

4. Conclusions

The gas sensing mechanisms for nanoporous NiO films modulated by UV and visible light irradiation were investigated by measuring the chemoresistive response and the surface reactions by *in situ* FTIR spectroscopy at various operating conditions. Two gases exhibiting different electron affinities were studied: NO$_2$ – a strongly oxidizing agent, and acetone – a nucleophilic molecule. Pronounced enhancement of the resistance change was observed upon NO$_2$ exposure and simultaneous illumination with light at a wavelength of 275 nm. Much smaller chemoresistive changes were observed using a longer wavelength. Since 275 nm was the only light energy exceeding the optical band gap, the enhancement was attributed to interband transition in NiO. *In situ* FTIR surface spectroscopy showed that surface nitro and nitrate species form upon NO$_2$ exposure in synthetic air. Optical interband transition promotes electron-stimulated surface nitro and nitrate ion formation and explains the accelerated and enhanced sensor response upon 275 nm illumination. For NO$_2$ sensing of NO$_x$ in air, we find that there is a fundamental reason why the UV-induced response of NiO is not very dramatic for NO$_2$, or even absent after stabilizing it in NO$_2$. UV light does the same as dark adsorption, and merely accelerates the surface reactions of NO$_2$ into nitro and nitrate species, which explains the result in Figs. 5 and 6. We thus conclude that enhanced light-induced sensor

responses of MOS cannot always be expected for reactive gas sensing. The FTIR results support a surface reaction model that maintains a steady-state coverage of nitro and nitrate species that reversibly replenish surface sites to allow repeated NO$_2$ sensing over many cycles. The resistive change of the NiO sensor was increased at an operating temperature of 150 °C compared to room temperature operation. Notably, the NiO sensor showed a stable response to NO$_2$ in humidified gas, unlike typical *n*-type MOS gas sensors due to the strong oxidizing character of NO$_2$, which governs the minority charge carrier concentration reactions and the overall surface reaction. Hence, water does not affect the majority hole conduction; only the rate at which steady-state condition is established.

In the case of acetone, an increased sensor resistance without noticeable effects of either temperature or illumination was observed. *In situ* FTIR spectroscopy shows that acetone exposure leads to irreversible decomposition into formate and methoxy species covering the surface and limiting gas sensing.

The presented results clarify the mechanism of NiO for NO$_2$ gas sensing and explain both the reversible cycling and humidity tolerance and its responsivity enhancement upon simultaneous bandgap illumination. Further enhancement of the limits of detection down to low-ppb with maintained stability and humidity tolerance compromises increased porosity and maintained nanocrystallinity. Further decomposition of acetone and gradual deactivation of the NiO surface suggests that adding an oxidizing noble metal co-catalyst would improve the sustained NiO gas sensor responsivity.

We emphasize that it is still an open question how the studied NiO sensors respond to other gases, which are important for potential practical applications, when the NiO sensor is irradiated. However, we expect that the response to SO$_2$ gas will be similar to NO$_2$, based on our previous studies [40].

CRediT authorship contribution statement

Katarzyna Drozdowska established and ran the experimental electrical studies, evaluated DL analysis. **Tesfalem Welearegay** fabricated and characterized the NiO samples and performed the *in situ* FTIR spectroscopy together with **Lars Österlund**. **Lars Österlund** and **Janusz Smulko** participated in data analysis. **Lars Österlund** interpreted FTIR spectroscopy results. **All Authors** wrote the manuscript.

Declaration of Competing Interest

The authors declare that they have no known competing financial interests or personal relationships that could have appeared to influence the work reported in this paper.

Acknowledgments

Appendix A. Supplementary material

References

[1] P.T. Moseley, Progress in the development of semiconducting metal oxide gas sensors: a review, Meas. Sci. Technol. 28 (2017), https://doi.org/10.1088/1361-6501/aa7443.

[2] A. Dey, Semiconductor metal oxide gas sensors: a review, Mater. Sci. Eng. B Solid-State Mater. Adv. Technol. 229 (2018) 206–217, https://doi.org/10.1016/j.mseb.2017.12.036.

[3] C. Wang, L. Yin, L. Zhang, D. Xiang, R. Gao, Metal oxide gas sensors: sensitivity and influencing factors, Sensors 10 (2010) 2088–2106, https://doi.org/10.3390/s100302088.

[4] J. Li, D. Gu, Y. Yang, H. Du, X. Li, UV light activated SnO2/ZnO nanofibers for gas sensing at room temperature, Front. Mater. 6 (2019), https://doi.org/10.3389/fmats.2019.00158.

[5] H.J. Choi, S.H. Kwon, W.S. Lee, K.G. Im, T.H. Kim, B.R. Noh, S. Park, S. Oh, K. K. Kim, Ultraviolet photoactivated room temperature NO2 gas sensor of ZnO hemitubes and nanotubes covered with TiO2 nanoparticles, Nanomaterials 10 (2020), https://doi.org/10.3390/nano10030462.

[6] G.F. Fine, L.M. Cavanagh, A. Afonja, R. Binions, Metal oxide semi-conductor gas sensors in environmental monitoring, Sensors 10 (2010) 5469–5502, https://doi.org/10.3390/s100605469.

[7] I. Kortidis, H.C. Swart, S.S. Ray, D.E. Motaung, Characteristics of point defects on the room temperature ferromagnetic and highly NO2 selectivity gas sensing of p-type Mn3O4 nanorods, Sens. Actuators B Chem. 285 (2019) 92–107, https://doi.org/10.1016/j.snb.2019.01.007.

[8] R.L. Wilson, C.E. Simion, A. Stanoiu, A. Taylor, S. Guldin, J.A. Covington, C. J. Carmalt, C.S. Blackman, Humidity-tolerant ultrathin NiO gas-sensing films, ACS Sens. 5 (2020) 1389–1397, https://doi.org/10.1021/acssensors.0c00172.

[9] T.P. Mokoena, H.C. Swart, D.E. Motaung, A review on recent progress of p-type nickel oxide based gas sensors: future perspectives, J. Alloy. Compd. 805 (2019) 267–294, https://doi.org/10.1016/j.jallcom.2019.06.329.

[10] H.J. Kim, J.H. Lee, Highly sensitive and selective gas sensors using p-type oxide semiconductors: overview, Sens. Actuators B Chem. 192 (2014) 607–627, https://doi.org/10.1016/j.snb.2013.11.005.

[11] D.N. Oosthuizen, D.E. Motaung, H.C. Swart, Selective detection of CO at room temperature with CuO nanoplatelets sensor for indoor air quality monitoring manifested by crystallinity, Appl. Surf. Sci. 466 (2019) 545–553, https://doi.org/10.1016/j.apsusc.2018.09.219.

[12] Y. Yu, Y. Xia, W. Zeng, R. Liu, Synthesis of multiple networked NiO nanostructures for enhanced gas sensing performance, Mater. Lett. 206 (2017) 80–83, https://doi.org/10.1016/j.matlet.2017.06.119.

[13] R. Miao, W. Zeng, Q. Gao, SDS-assisted hydrothermal synthesis of NiO flake-flower architectures with enhanced gas-sensing properties, Appl. Surf. Sci. 384 (2016) 304–310, https://doi.org/10.1016/j.apsusc.2016.05.070.

[14] C. Su, L. Zhang, Y. Han, C. Ren, X. Chen, J. Hu, M. Zeng, N. Hu, Y. Su, Z. Zhou, Z. Yang, Controllable synthesis of crescent-shaped porous NiO nanoplates for conductometric ethanol gas sensors, Sens. Actuators B Chem. 296 (2019), 126642, https://doi.org/10.1016/j.snb.2019.126642.

[15] X. Lai, G. Shen, P. Xue, B. Yan, H. Wang, P. Li, W. Xia, J. Fang, Ordered mesoporous NiO with thin pore walls and its enhanced sensing performance for formaldehyde, Nanoscale 7 (2015) 4005–4012, https://doi.org/10.1039/c4nr05772d.

[16] E. Espid, F. Taghipour, UV-LED photo-activated chemical gas sensors: a review, Crit. Rev. Solid State Mater. Sci. 42 (2017) 416–432, https://doi.org/10.1080/10408436.2016.1226161.

[17] A. Chizhov, M. Rumyantseva, A. Gaskov, Light activation of nanocrystalline metal oxides for gas sensing: principles, achievements, challenges, Nanomaterials 11 (2021), https://doi.org/10.3390/nano11040892.

[18] J. Wang, H. Shen, Y. Xia, S. Komarneni, Light-activated room-temperature gas sensors based on metal oxide nanostructures: a review on recent advances, Ceram. Int. (2020), https://doi.org/10.1016/j.ceramint.2020.11.187.

[19] F. Xu, H.P. Ho, Light-activated metal oxide gas sensors: a review, Micromachines 8 (2017), https://doi.org/10.3390/mi8110333.

[20] M.D. Irwin, D.B. Buchholz, A.W. Hains, R.P.H. Chang, T.J. Marks, p-Type semiconducting nickel oxide as an efficiency-enhancing anode interfacial layer in polymer bulk-heterojunction solar cells, Proc. Natl. Acad. Sci. USA 105 (2008) 2783–2787, https://doi.org/10.1073/pnas.0711990105.

[21] X. Geng, D. Lahem, C. Zhang, C.J. Li, M.G. Olivier, M. Debliquy, Visible light enhanced black NiO sensors for ppb-level NO2 detection at room temperature, Ceram. Int. 45 (2019) 4253–4261, https://doi.org/10.1016/j.ceramint.2018.11.097.

[22] C.G. Granqvist, R.A. Buhrman, Ultrafine metal particles, J. Appl. Phys. 47 (1976) 2200–2219, https://doi.org/10.1063/1.322870.

[23] T.G. Welearegay, U. Cindemir, L. Österlund, R. Ionescu, Fabrication and characterisation of ligand-functionalised ultrapure monodispersed metal nanoparticle nanoassemblies employing advanced gas deposition technique, Nanotechnology 29 (2018), https://doi.org/10.1088/1361-6528/aa9f65.

[24] U. Cindemir, Z. Topalian, C.G. Granqvist, L. Österlund, G.A. Niklasson, Characterization of nanocrystalline-nanoporous nickel oxide thin films prepared by reactive advanced gas deposition, Mater. Chem. Phys. 227 (2019) 98–104, https://doi.org/10.1016/j.matchemphys.2019.01.058.

[25] R. Karsthof, H. von Wenckstern, J. Zúñiga-Pérez, C. Deparis, M. Grundmann, Nickel oxide–based heterostructures with large band offsets, Phys. Status Solidi 257 (2020), 1900639, https://doi.org/10.1002/PSSB.201900639.

[26] A. Mattsson, M. Leideborg, K. Larsson, G. Westing, L. Österlund, Adsorption and solar light decomposition of acetone on anatase TiO2 and niobium doped TiO2 thin films, J. Phys. Chem. B 110 (2006) 1210–1220, https://doi.org/10.1021/jp055656z.

[27] A.P. Grosvenor, M.C. Biesinger, R.S.C. Smart, N.S. McIntyre, New interpretations of XPS spectra of nickel metal and oxides, Surf. Sci. 600 (2006) 1771–1779, https://doi.org/10.1016/J.SUSC.2006.01.041.

[28] M. Urso, S.G. Leonardi, G. Neri, S. Petralia, S. Conoci, F. Priolo, S. Mirabella, Room temperature detection and modelling of sub-ppm NO2 by low-cost nanoporous NiO film, Sens. Actuators B Chem. 305 (2020), 127481, https://doi.org/10.1016/j.snb.2019.127481.

[29] M. Procek, A. Stolarczyk, T. Pustelny, Impact of temperature and UV irradiation on dynamics of NO2 sensors based on ZnO nanostructures, Nanomaterials 7 (2017), https://doi.org/10.3390/nano7100312.

[30] D.E. Tevault, L. Andrews, Laser Raman matrix isolation studies of nitrogen dioxide. Resonance Raman spectrum of NO2 and Raman spectrum of N2O4, Spectrochim. Acta Part A Mol. Spectrosc. 30 (1974) 969–975, https://doi.org/10.1016/0584-8539(74)80013-9.

[31] A.A. Davydov, Infrared Spectroscopy of Adsorbed Species on the Surface of Transition Metal Oxides, Wiley, 1991, https://doi.org/10.1002/bbpc.19910950424.

[32] B. Wang, J. Nisar, R. Ahuja, Molecular simulation for gas adsorption at NiO (100) surface, ACS Appl. Mater. Interfaces 4 (2012) 5691–5697, https://doi.org/10.1021/am3016894.

[33] G.B. Deacon, R.J. Phillips, Relationships between the carbon-oxygen stretching frequencies of carboxylato complexes and the type of carboxylate coordination, Coord. Chem. Rev. 33 (1980) 227–250, https://doi.org/10.1016/S0010-8545(00)80455-5.

[34] N. Nishino, B.J. Finlayson-Pitts, Thermal and photochemical reactions of NO2 on chromium(iii) oxide surfaces at atmospheric pressure, Phys. Chem. Chem. Phys. 14 (2012) 15840–15848, https://doi.org/10.1039/c2cp42292a.

[35] G.M. Underwood, T.M. Miller, V.H. Grassian, Transmission FT-IR and Knudsen cell study of the heterogeneous reactivity of gaseous nitrogen dioxide on mineral oxide particles, J. Phys. Chem. A 103 (1999) 6184–6190, https://doi.org/10.1021/jp991586i.

[36] R.V. Mikhaylov, A.A. Lisachenko, B.N. Shelimov, V.B. Kazansky, G. Martra, S. Coluccia, FTIR and TPD study of the room temperature interaction of a NO-oxygen mixture and of NO2 with titanium dioxide, J. Phys. Chem. C 117 (2013) 10345–10352, https://doi.org/10.1021/jp311593s.

[37] S. Zhao, Y. Shen, P. Zhou, J. Zhang, W. Zhang, X. Chen, D. Wei, P. Fang, Y. Shen, Highly selective NO2 sensor based on p-type nanocrystalline NiO thin films prepared by sol–gel dip coating, Ceram. Int. 44 (2018) 753–759, https://doi.org/10.1016/j.ceramint.2017.09.243.

[38] N.M. Hung, C.M. Hung, N. Van Duy, N.D. Hoa, H.S. Hong, T.K. Dang, N.N. Viet, L. V. Thong, P.H. Phuoc, N. Van Hieu, Significantly enhanced NO2 gas-sensing performance of nanojunction-networked SnO2 nanowires by pulsed UV-radiation, Sens. Actuators A Phys. 327 (2021), 112759, https://doi.org/10.1016/j.sna.2021.112759.

[39] L. Österlund, Fourier-transform infrared and Raman spectroscopy of pure and doped TiO2 photocatalysts, in: Sol. Hydrog. Nanotechnol., John Wiley and Sons, 2010, pp. 189–238, https://doi.org/10.1002/9780470823996.ch8.

[40] D. Langhammer, J. Kullgren, L. Österlund, Photoinduced adsorption and oxidation of SO2 on anatase TiO2(101), J. Am. Chem. Soc. 142 (2020) 21767–21774, https://doi.org/10.1021/JACS.0C09683.

Katarzyna Drozdowska received her M.Sc. degree in nanotechnology from Gdańsk University of Technology, Poland, in 2020. During her studies, she took a traineeship at Max Planck Institute for Polymer Research, Mainz, Germany (2018), where she investigated thin-film transistors based on organic substances. Currently, she is pursuing her Ph. D. studies at the Department of Metrology and Optoelectronics in the field of electronics. Her main research focus concerns low-dimensional materials for gas sensing devices, utilizing light modulation and 1/f noise for more sensitive and selective detection of volatile compounds.

Tesfalem Welearegay received his Ph.D. (2019) and M.Sc. (2013) Degree in Nanoscience and Nanotechnology from Rovira i Virgili University (Spain), and currently, he is a researcher at Ångström Laboratory, Department of Materials Science and Engineering, Uppsala University (Sweden). His research interests include micro and nanofabrication of metal nanoparticles and semiconductor metal oxide nanostructures for chemical gas sensing application, VOCs analysis in exhaled breath, and E-nose systems for non-invasive disease diagnosis.

Lars Österlund is professor and co-chair of Div. Solid State Physics at Uppsala University. He received his Ph.D. in 1997 from Chalmers University of Technology on photon-induced reactions on solid surfaces. He did his postdoc at Aarhus University in Denmark 1997–2000 on fundamental studies of adsorbate interactions on solid surfaces using vacuum and high-pressure scanning tunneling microscopy. He was employed as Assistant Professor at Chalmers 2000–2002 and obtained Docent title at Chalmers 2002. Between 2003 and 2009 he was research director at FOI – The Swedish Defence Research Institute and was thereafter appointed professor at Uppsala University. He is the co-founder of the Swedish Society of Vibrational Spectroscopy. He is a board member of the Uppsala Center for Photon Sciences, The Uppsala International Science Program, and the Transparent Conducting Materials network (TCMnet), and co-founder of two spin-offs in cleantech and medical technology. His current research focuses on catalytic nanomaterials, photo-electro-responsive and chromogenic materials, self-cleaning surfaces, and solid-state gas sensors with applications in air and water treatment, solar fuel, building technology, and medical technology. He has published 176 peer-reviewed scientific articles, book chapters and books, and holds 6 international patents.

Janusz Smulko received his M.Sc., Ph.D. and D.Sc. degrees in electronics from Gdańsk University of Technology, Poland, in 1989, 1996 and 2007, respectively. Presently, he is a full professor (since 2016), Head of the Metrology and Optoelectronics Department (since 2012). He had also conducted scientific research in short-term positions at Texas A&M University (2003), Uppsala University (2006/07), Massachusetts Institute of Technology (2011, 2013). As a researcher, he focuses on the applications of 1/f noise for gas sensing

and reliability assessment of electronic components and structures, the influence of noise on detection efficiency in Raman spectroscopy systems. He was Vice-Rector for Research of the Gdańsk University of Technology (in the term 2016–2019), member of the Committee on Metrology and Scientific Instrumentation of the Polish Academy of Science (two terms: 2013–2019) and Editor-in-Chief of Metrology and Measurement Systems Journal (two terms: 2013–2019), Chair of IEEE Chapter Computer Society Gdańsk (two terms: 2014–2017). Professor chaired three International Conferences on Noise and Fluctuations issues and managed seven research projects. He was a member of the H2020-MSCA-RISE-2014 project TROPSENSE: "Development of a non-invasive breath test for early diagnosis of tropical diseases" (No: 645758) and co-authored more than 120 papers.